Investigation of SERS Frequency Fluctuations Relevant to Sensing and Catalysis

Chelsea M. Zoltowski⁺, Deben N. Shoup⁺, and Zachary D. Schultz*

Department of Chemistry and Biochemistry, The Ohio State University, Columbus, OH 43210, USA

+ - Denotes equal author contribution
* corresponding author email: schultz.133@osu.edu

Abstract

The excitation of plasmon resonances on nanoparticles generates locally enhanced electric fields commonly used for sensing applications and energetic charge carriers can drive chemical transformations as photocatalysts. The surface-enhanced Raman scattering (SERS) spectra from mercaptobenzoic acid (MBA) adsorbed to gold nanoparticles (AuNP) and silica encapsulated gold nanoparticles (AuNP@silica) can be used to assess the impact of energetic charge carriers on the observed signal. Measurements were recorded using a traditional point focused Raman spectroscopy and a wide-field spectral imaging approach to assess changes in the spectra of the different particles at increasing power density. The wide-field approach provides an increase in sampling statistics and shows evidence of SERS frequency fluctuations from MBA at low power densities, where it is commonly difficult to record spectra from a point focused spot. The increased spectral resolution of the point spectroscopy measurement provides improved peak identification and the ability to correlate the frequency fluctuations to charged intermediate species. Interestingly, our work suggests that isolated nanoparticles may undergo frequency fluctuations more readily than aggregates.

Introduction

The excitation of plasmon resonances in nanomaterials has generated exciting possibilities in diverse applications from sensing to catalysis.¹⁻⁴ The observation of increased Raman signals from nanostructured surfaces and subsequent recognition of the enhanced Raman signals has driven research into these interactions.⁵⁻⁶ The enhancement of the Raman signal, known as surface-enhanced Raman scattering (SERS), was correlated with the excitation of a localized surface plasmon resonance (LSPR),⁷ which is dependent on the excitation wavelength as well as the structure of the metal surface. Arguably, the recognition that plasmon resonances mediated the enhanced Raman response, the electromagnetic enhancement mechanism, initiated increased interest in the optical properties of plasmonic nanomaterials. These properties have since been linked to the generation of energetic charge carriers for photocatalysis,⁸ and remain active areas of research.^{1,9-13}

Excitation of the LSPR of metal nanostructures can create hot carriers that can be transferred through three mechanisms: indirect charge transfer, direct intramolecular excitation, and direct charge transfer. Indirect charge transfer results from nonradiative decay of the LSPR. Direct intramolecular transfer occurs when the hot-electron is generated from direct excitation of the LSPR from the highest occupied molecular orbital (HOMO) to the lowest unoccupied molecular orbital (LUMO) of the molecule adsorbed to the metal nanostructure. Lastly, direct charge transfer occurs when hot-electrons are resonantly transferred from the metal to the LUMO adsorbed molecule. ¹⁴Direct charge transfer can also contribute to an increase in SERS signal. Polymethine dyes have been reported to experience the direct charge transfer mechanism of hot carriers contributing to a resonance Raman chemical enhancement and thus an increased SERS signal. ¹⁵

Hot carrier generation can be detected in the SERS spectrum, providing molecular specificity for monitoring catalytic reactions. An example of using SERS in conjunction with hot carrier formation for catalytic reactions includes inducing oxidation or reduction reactions, such as the reduction of carbon dioxide. Hot carriers also have the ability to induce additional chemical transformations such as dimerization or crosslinking which alter the observed SERS spectrum. The dimerization of *para*-aminothiophenol (PATP) to 4,4'-dimeraptoazobenzene (DMAB) is a commonly studied example. Originally, excitation wavelength and potential dependent bands were attributed to b2 modes of PATP until it was shown those bands were the result of dimerization of PATP to DMAB. Additional azo-bridge formations have also been reported as the result of hot-carrier generation in SERS. The effects of hot carriers have also been seen in tip enhanced Raman spectroscopy (TERS), where the plasmonic properties of nanoparticles on the coated apex of an atomic force microscopy tip allows for spatial monitoring of hot carrier catalysis. ²¹

The ability to monitor catalytic and chemical transformations through hot carrier generation with SERS is advantageous. SERS intensity fluctuations (SIFS) can appear as "blinking" in the emission of light from the nanomaterial.²²⁻²³ Blinking effects have been reported by multiple groups who have aimed to determine the mechanisms behind the fluctuations. Spectral fluctuations can alter the observed frequencies and intensities through transient interactions with hot carriers.²⁴⁻²⁵ Previous SERS reports of bovine serum albumin (BSA) with gold nanoparticles have acknowledged spectral intensity and frequency fluctuations to which they attribute to varying conformations of BSA on the nanoparticles resulting in different amino acid residues being enhanced.²⁶ However, our group, as well as others, have previously identified the formation of

radical anion species resulting from hot carrier transfer to analytes of interest including tryptophan and 4-4'-bipyridine molecules resulting in temporal spectral and intensity fluctuations. ²⁷⁻²⁹ Density functional theory (DFT) calculations are commonly used in support for formation of radical species to simulate the Raman spectrum of the observed intermediates. ³⁰⁻³² TERS experiments also report similar temporal signal fluctuations resulting from transient species chemically formed from hot carriers. Previous reports have monitored a hot carrier induced transformation of 4-nitrobenzene thiol (4-NBT) conversion to 4-NBT thiolate, resulting in temporal fluctuations in the TERS spectra. ²¹ Other temporal transient species reported with TERS includes photofragmentation of thiophenol as well as the polycyclic intermediates resulting in frequency fluctuations between 1350-1600 cm⁻¹. ²¹

For chemical sensing, avoiding these hot-carrier analyte interactions can be important, while these same interactions may be key for initiating chemical transformations. In sensing, it has been established that controlling the energy associated with the plasmon resonance is important for avoiding photodamage. The electric field difference between nanoparticle monomers and dimers is also known to impact the observed signal. The ability to identify the interactions occurring to differentiate hot carrier effects from the signal of specific analytes remains an important challenge. In this paper we explore two methods of acquiring the SERS signal from the common Raman reporter molecule, 4-mercaptobenzoic acid (MBA) to monitor for signal fluctuations and assess their impact on the average SERS signal observed. Using traditional point focused Raman spectroscopy, high resolution spectra are acquired with increasing power density. We correlate these observations with wide-field, spectral imaging of the same samples, where additional information can be obtained. We identify the formation of transient chemical species from hot carriers at low power density typical of SERS and assign transient spectra observed to charged intermediates.

Methods

Materials

Hydrogen tetrachloroaurate(III) hydrate (HAuCl₄), sodium citrate tribasic dihydrate, 4-mercaptobenzoic acid (MBA), ethanol, ammonium hydroxide, isopropanol (IPA), and tetraethyl orthosilicate (TEOS) were obtained from Sigma-Aldrich and used as received.

AuNP Synthesis

Gold nanoparticles (AuNPs) were synthesized using a citrate reduction method.³⁵ Briefly, 0.4 mM HAuCl₄ in water was heated to boiling while stirring. 1 mL of 50 mM sodium citrate was added to the solution. The solution remained heating and stirred for 15 minutes until the solution changed to a red color and then was left stirring until cool. The resulting AuNPs were characterized using UV-Vis, Dynamic light scattering (DLS), and a Snowy Range IM-52 Raman spectrometer at 638 nm. The observed UV-Visible extinction spectrum is shown in **Figure S1**.

MBA functionalization of AuNP

Synthesized AuNPs (53 nm by DLS) were centrifuged for 20 minutes at 6000 rpm, and the supernatant was decanted to remove excess citrate. The pelleted particles were resuspended in 1 mL of H_2O . 10 μL of 40 mM mercaptobenzoic acid (MBA) was added to each 1 mL vial of particles and shaken for 40 mins. These particles were centrifuged again for 20 mins at 6000 rpm

and pelleted to remove access MBA. Once the supernatant was removed each vial was resuspended in 1 mL of H₂O. The MBA functionalized AuNPs were characterized using UV-Vis (**Figure S1A**) and a Snowy Range IM-52 Raman spectrometer at 638 nm (**Figure S1B**). 30 μL of functionalized particles were dropped on a glass slide and covered with a cover slip and allowed to dry.

Silica encapsulation of MBA functionalized AuNPs, AuNP@silica

Synthesized AuNPs (40 nm by DLS) were functionalized with MBA by adding 100 μ L of 40 mM MBA to 10 mL of the NP suspension. The solution then shook for 30 minutes, was pelleted, the supernatant removed, and then resuspended in 2 mL of water. To encapsulate the MBA functionalized AuNPs with silica, 6 mL EtOH and 0.4 mL NH4OH were added to the AuNP solution. This solution was added to 20 mL IPA, 20 μ L TEOS, and 0.3 mL of water and shook for 19 hours. This solution was pelleted by centrifugation for 30 minutes at 3000 g. The pellet was twice washed in 1 mL of of 1:1 EtOH: water and centrifuged for 20 minutes at 3000 g and resuspended in 2 mL water. The MBA functionalized AuNP@silica were characterized using UV-Vis (**Figure S1A**) and a Snowy Range IM-52 Raman spectrometer at 638 nm (**Figure S1B**). 30 μ L of AuNP@silica were dropped on a glass slide and covered with a cover slip and allowed to dry. TEM analysis of the synthesized particles is shown in **Figure S2**.

Point spectroscopy experiments

Raman spectroscopy was performed using a home-built instrument with a 640 nm laser (Oxxius). The laser was focused onto the sample slides using a 40x water immersion objective (NA=0.8). Raman scattering was collected through the same objective and directed to an Isoplane SCT320 spectrograph equipped with a ProEM: 1600^2 eXcelon 3 CCD detector (Princeton Instruments). 1000 spectra were acquired with an exposure time of 10 ms using various laser powers at the sample.

The power density for point spectroscopy measurements was determined by monitoring the change in intensity from the 520 cm⁻¹ Si phonon on a patterned silicon sample. The laser was focused onto slide with a sharp line between regions of Si and gold as shown in **Figure S3A**. The sample was translated in 1 µm increments across the Au/Si boundary, and 1 s acquisitions at each position as the laser focus was moved from the gold to the silica. The experiment was repeated at laser powers of 2 mW and 8 mW measured at the surface as shown in **Figure S3B** and **Figure S3C** respectively. The observed intensities on the Si and Au regions were fit with a line and the laser spot sized was determined from the width of the observed transition, which included the endpoint of each plateau and any points in the middle. Measurements at both 2 and 8 mW indicate a 2 µm laser spot, corresponding to power densities at the surface ranging from 64 to 215 kW/cm², respectively.

Wide-field spectral imaging experiments

Prior to imaging, solutions of the AuNPs and AuNP@silica were dropped onto glass slides and allowed to dry. An inverted microscope (IX-71, Olympus) with a 100x, 1.3 NA oil immersion objective (Olympus) was used for wide-field imaging. A 659 nm single longitudinal mode diode laser (Laser Quantum) was directed through a plano-convex lens (Thorlabs) positioned at its focal length (f=75 mm) above the sample to produce a 30 µm laser spot on the sample. The collected light was directed through a 638 nm long pass dichroic mirror (Thorlabs) and a 660 nm long pass edge filter (Semrock) situated in a microscope filter cube (Thorlabs) and then through a 300

groove/mm visible transmission diffraction grating with a 17.5° blaze angle (Thorlabs) and onto a 2-dimensional scientific complementary oxide semiconductor (sCMOS) detector (ORCA-Flash 4.0 V2, Hamamatsu, LTD). Images were acquired at a 100 ms (10 Hz) frame rate for 1000 frames. Polarization dependent experiments were conducted by placing a polarization filter followed by a $\lambda/2$ waveplate (Thorlabs) in the optical path prior to the sample. The $\lambda/2$ waveplate was rotated in fixed increments to rotate the incident polarization in the sample plane. Polarization dependent images were acquired at a 10 Hz frame rate for 100 frames. Pixel position on the sCMOS was calibrated to wavelength and Raman shift by imaging a neon calibration lamp (Newport) directed through a 1 μ m pinhole (Thorlabs) as described previously.^{24, 36} Data was acquired using the NIS-Elements Advanced Research software (Nikon).

Data processing

ImageJ (U.S. National Institutes of Health) was used for image analysis for data obtained from the wide field experiments and Matlab (Mathworks) was used for spectral analysis. For each nanoparticle, the rows of pixels containing the spectral features were averaged together to generate spectra from the images, as described previously.³⁶ The spectra from all 1000 image frames collected were used to generate spectral heat maps for individual nanoparticles.

Results

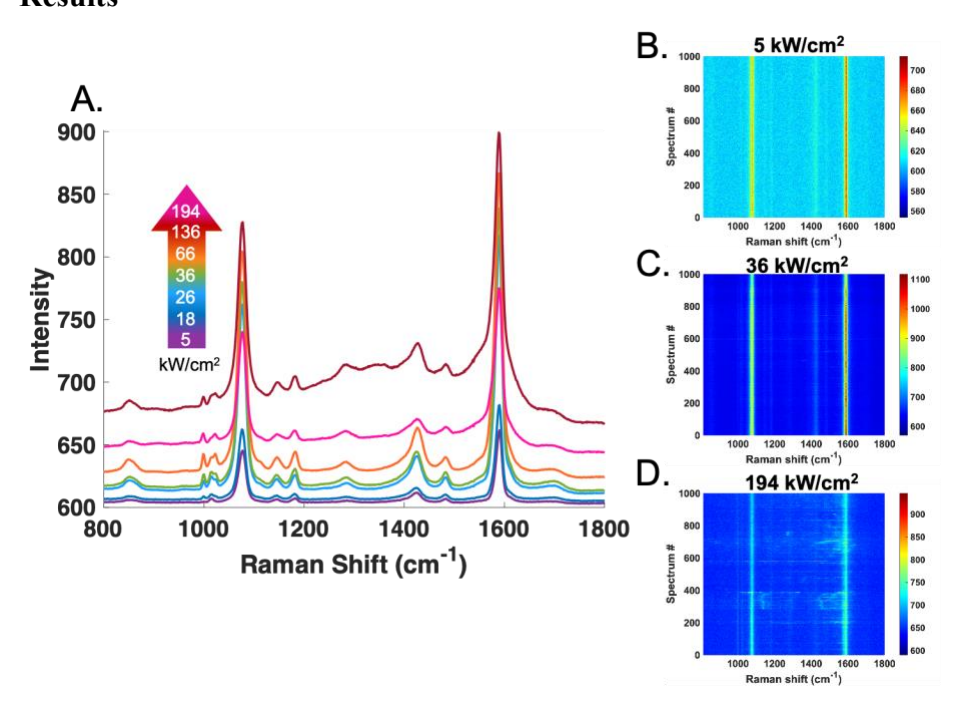


Figure 1: Point spectroscopy on MBA functionalized AuNP A) Mean MBA signal from AuNP for 5000 spectra obtained at increasing power densities. The spectra shown at each power density are the average of 1000x 10 ms acquisitions from 5 different locations. The power density is calculated from the power measured at the spot and the experimentally determined spot size. B-D) The heat maps plot the 1000 consecutive spectra obtained from a single spot acquired at 5 kW/cm^2 (B), 36 kW/cm^2 (C), and 194 kW/cm^2 (D).

Figure 1 shows the SERS spectrum arising from MBA adsorbed to AuNPs at increasing excitation laser power density. An image of the AuNPs dispersed in the microscope's field of view (FOV) is provided in **Figure S4.** At each power density, 1000, 10 ms spectra were acquired at 5

spots, to excite particles from different areas on the sample. The mean spectra from the data acquired at each power density are shown in Figure 1A. In this figure, there is an increase in the background as power density increases until a power density of 136 kW/cm². At the highest power density (194 kw/cm²), the background and SERS signal is observed to decrease slightly. The average spectrum acquired at 136 kW/cm² show a disproportionate increase in the background between 1200 and 1400 cm⁻¹, which is characteristic of the formation of carbonaceous products from burning the molecule at the surface.³⁷ At each power density, the expected vibrational assignments of MBA at 1074 and 1590 cm⁻¹, attributed to ring breathing modes, ³⁸ are the most dominant features observed and increase with the power density. Aside from the expected MBA peaks, a peak at 1427 cm⁻¹ is present in varying intensities in the mean ensemble at each power density. The peak at 1427 cm⁻¹ appears to arise from the interaction of MBA carboxylate moiety with the silica as it is not observed in the ensemble SERS spectrum of the MBA functionalized AuNP in solution but is evident in the ensemble solution spectra with a silica shell, Figure S1. When the MBA functionalized AuNPs are deposited on a glass surface and dried, the feature is again observed, further supporting an interaction with silica. Doublet peaks located at 1000 and 1023 cm⁻¹ appear to increase with the first four increasing power densities; however, it is not obvious there is a consistent increase in intensity of these peaks after 36 kW/cm². These doublet peaks have been previously associated with the thiophenol biproduct from the decarboxylation of MBA.39-40

The average spectra provide ensemble information at each power density; however, analysis of the individual spectra acquired at each spot at each power density reveals additional transient events. Representative heat maps constructed from the 1000 spectra acquired at one spot for the lowest (5 kW/cm²), a moderate (36 kW/cm²), and the highest (194 kW/cm²) power density are shown in **Figure 1B-D**, respectively. Each heat map shows the expected MBA peaks dominate the majority of the spectra acquired. As the power density increases, vibrational fluctuations are observed in spectra at various time points. Spectral fluctuations are uncommon at the low power density. In **Figure 1C**, the heat map corresponds to a spot at 36 kW/cm² and some low intensity fluctuations are observed. At higher power density, such as 194 kw/cm² shown in **Figure 1D**, fluctuations are more frequent and intense.

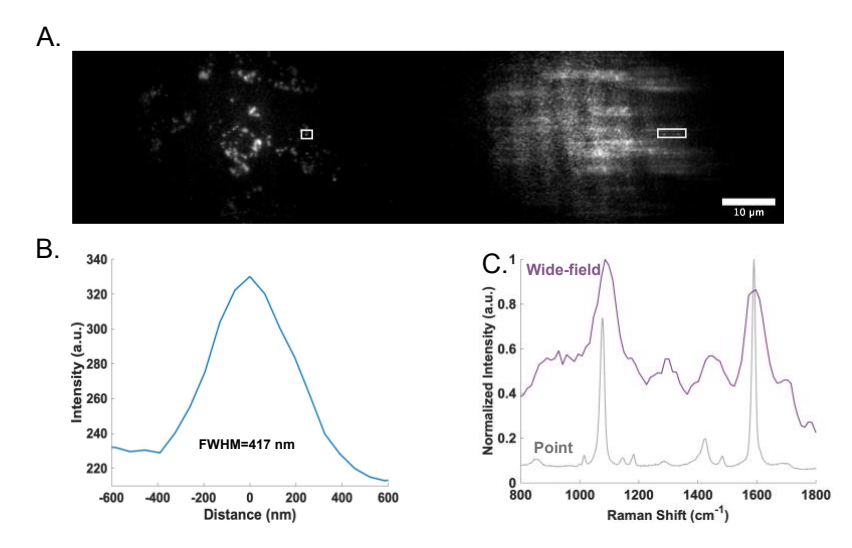


Figure 2. Wide-field spectrally resolved imaging of MBA functionalized AuNPs. A) The average image of AuNP nanoparticles image constructed from 1000 frames collected at 10 Hz with a power density of 0.93 kW/cm². The collected signal is dispersed with a transmission diffraction gratin and the image of the AuNPs (n=0, left) and the wavelength dispersed first-order diffraction signal (n=1, right) are collected on the sensor as shown. A particle of interest, both n=0 and n=1 response, is indicated by the boxes. B) The intensity profile of the n=0 image of the nanoparticle of interest is shown. C) The average MBA spectrum from the particle of interest in the wide-field experiment (top, purple) is compared with the average MBA spectrum at 5 kW/cm² from the point spectral imaging experiment (bottom, grey).

Wide field imaging enables a large number of nanoparticles to be excited simultaneously and can avoid selection bias associated with sampling in point spectroscopy approaches. Figure 2 shows results from a wide field spectral imaging setup utilized to analyze MBA functionalized AuNP. This imaging approach disperses the collected signal into the n=0 order diffraction (providing a spatial image) and n=1 order diffraction (a spectrally resolved image) allowing for simultaneous nanoparticle imaging and Raman spectroscopy from multiple nanoparticles within a 30 µm FOV. 36 We note that the spectrum of particles on the same row of pixels can overlap in the n=1 portion of the image if not sufficiently far apart. The spectrum from aggregates or particles in adjacent pixels that image as single feature can be recorded with slightly lower spectral resolution as reported previously.³⁶ Unlike with the point spectroscopy setup, the spectral response can be associated with individual particles, dimers, or aggregated particles (Figure S5). Figure 2A is an example of AuNPs imaged (n=0) on the left and their spectral response (n=1) on the right. The boxes in Figure 2A indicate the particle and spectral response used for Figure 2B and 2C. The full width at half maximum (FWHM) and the symmetry of the intensity profile can indicate if a specific particle is a single particle or an aggregate. The intensity profile of a particle from the n=0 order, shown in Figure 2B, corresponds to a FWHM of 414 nm. This FWHM of the observed point spread function (psf) is larger than the diffraction limited size of 255 nm. In Figure 2B, there is a slight shoulder in the intensity profile of the psf that suggests the particle is a dimer or larger aggregate. The same analysis was performed on 3 types of particles observed in the samples and compared to one another, which are shown in Figure S5. The observed psf varies from symmetric in both directions as expected for a single particle, to elongated along one axis suggesting a dimer or elongated aggregate, to asymmetric patterns from aggregates. In addition to plotting the psf, we have tracked the polarization dependence of the scattering from the particles (Figure S6). It is possible that a dimer or small aggregate could evince a symmetric psf; in these

cases, aligning the incident polarization along the coupled particles is expected to enhance the emission. **Figure S6** shows the polarization dependence observed from particles that have symmetric psf; however, the polarization dependence of the scattering intensity enables us to distinguish monomers for small aggregates. **Figure 2C** shows the comparison of an average spectrum obtained at 0.93 kW/cm² of the particle indicated in **Figure 2A** using wide field spectral imaging compared to an average spectrum obtained at 5 kW/cm² using point spectroscopy. It was challenging to obtain signal in point spectroscopy experiments at the equivalent low power density, likely associated with locating and focusing the laser on the appropriate spot. The expected MBA peaks at 1074 and 1590 cm⁻¹ are apparent in the wide field spectrum; however, the spectral resolution in the wide field imaging is limited by the geometric constraints to capture both n=0 and n=1 diffraction on the sensor. The spectral resolution is limited by the size of the nanoparticles, the groove density transmission diffraction grating, and the short distance needed to fit the n=0 and n=1 signal on the camera sensor.³⁶

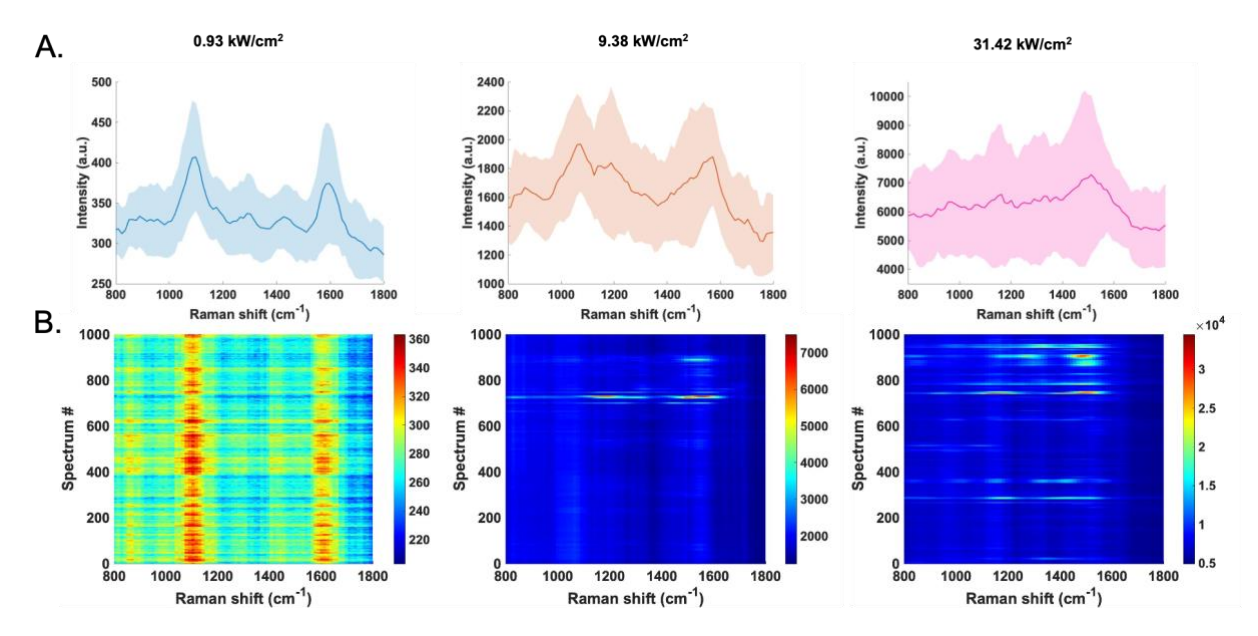


Figure 3: A) The mean spectrum obtained from MBA functionalized AuNPs at 0.93 (blue), 9.38 (orange), and 31.42 kW/cm² (pink) power densities are shown. The spectra shown are the average of 5 individual AuNPs, where 1000 acquisitions of 100 ms were acquired for each particle. B) A corresponding heat map showing frequency and intensity fluctuations from a representative particle (1000, 100 ms acquisitions) at each power density is shown.

Wide-field spectral imaging of AuNPs was performed at a range of power densities similar to the point spectroscopy experiment. At each power density, 1000 frames were acquired with a 100 ms frame rate. Each frame contains multiple particles within the FOV and the corresponding Raman spectrum for each particle. **Figure 3A** shows the mean spectrum derived from 5 particles (a total of 5000 spectra) at three power densities; the lowest at 0.93 kW/cm², a middle power density at 9.38 kW/cm², and the highest at 31.42 kW/cm². The power density in the wide-field experiments was limited by the laser output illuminating a larger FOV relative to concentrated focus in point spectroscopy measurements. In the wide-field approach, the expected MBA peaks at 1074 and 1590 cm⁻¹ are apparent at powers that were challenging to record signals in point

spectroscopy experiments. As the power density is increased to 9.38 (orange) and 31.42 kW/cm² (pink), the mean spectra begin to vary from the expected MBA signal. The expected MBA peaks become broader at the intermediate power density and are no longer apparent at the highest power density, indicating the spectrum is dominated by high intensity frequency fluctuations observed during acquisition. The standard deviation is shown as the shaded region of each mean spectrum plot and increases with increasing power density, supporting larger fluctuations in these signals.

Figure 3B shows a heat map of 1000 spectra obtained from a representative particle for each power density for which the mean is plotted. At a power density of 0.93 kW/cm² intensity fluctuations of the 1074 and 1590 cm⁻¹ peaks are observed in the heat map, but no frequency fluctuations occur. As the power density is increased to 9.38 kW/cm², frequency fluctuations dominate the intense spectra at later time points, but the 1074 and 1590 cm⁻¹ peaks can be seen with lower intensities. When the highest power density for this technique is reached at 31.41 kW/cm² the frequency fluctuations dominate the spectra and are more intense than the expected signals observed from MBA making the MBA peaks at 1074 and 1590 cm⁻¹ no longer apparent. The frequency fluctuations can be better observed with this setup by analyzing particles that are blinking as shown in the videos provided in **Supporting Video S1 and S2.**

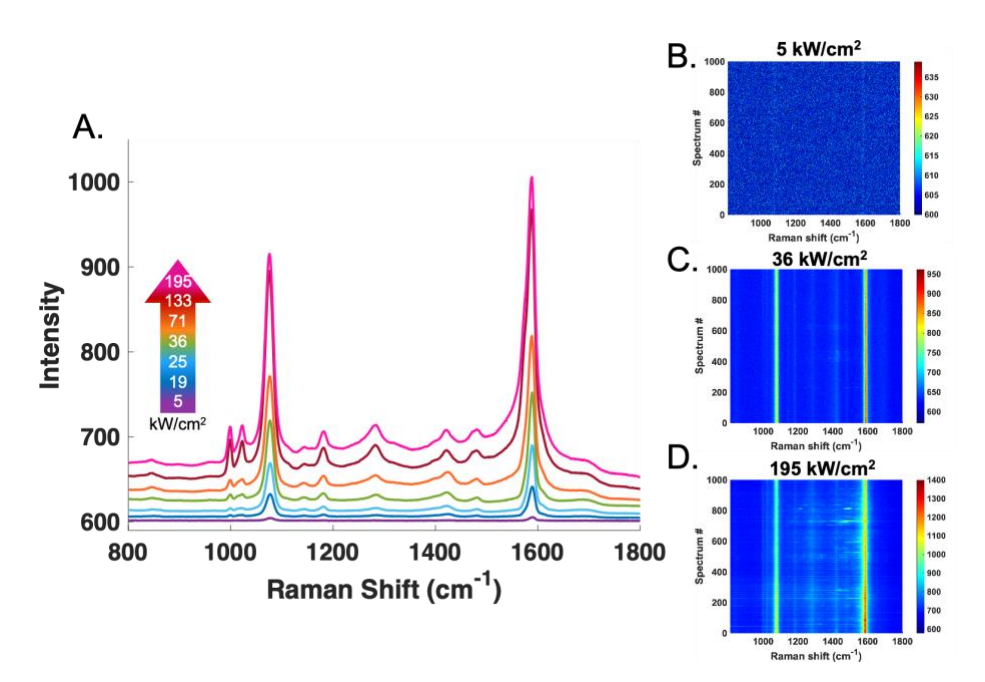


Figure 4: Point spectroscopy on MBA functionalized AuNP@silica A) Mean MBA signal from AuNP@silica derived from spectra obtained at increasing power densities are plotted. The spectra shown at each power density are the average of 1000x, 10 ms acquisitions from 5 different locations. The power density is calculated from the power measured at the spot and the experimentally determined spot size. B-D) The heat maps plot the 1000 consecutive spectra obtained from a single spot acquired at 5 kW/cm² (B), 36 kW/cm² (C), and 195 kW/cm² (D).

Gold nanoparticles encapsulated in silica (AuNP@silica) were used to analyze the impact of silica encapsulation on frequency fluctuations. These particles consist of gold NP cores that are functionalized with MBA and further encapsulated with a silica shell. Based on the TEM images shown in **Figure S2**, and additional TEM images not shown, the silica encapsulated particles

predominantly consist of single AuNP cores (88%), dimer AuNP cores (7%), and some larger aggregates (5%). Polarization dependent wide-field imaging (Figure S6) indicates a majority of monomers, consistent with TEM results. The microscope FOV for the dispersed AuNP@silica is provided in **Figure S7.** At each power density, 5 spots were chosen to excite varying particles. At each spot, 1000 spectra were acquired for 10 ms each. Figure 4A shows the mean of the 5000 spectra acquired at each power density. Similar to the MBA functionalized AuNP mean spectra (Figure 1A), the overall background increases with increasing power density. The AuNP@silica mean spectra show less background between 1200 and 1400 cm⁻¹ associated with carbonaceous species, indicating less photodamage is occurring with the silica encapsulation. Again, there are consistent peaks at 1074 and 1590 cm⁻¹ that are associated with the expected MBA Raman signal that increase in intensity with increasing power density. The peaks at 1074 and 1590 cm⁻¹ shown in Figure 4A are less intense at lower comparable power densities (5 and 19 kW/cm²) with the silica encapsulation than the bare AuNPs (Figure 1A). The particles encapsulated with silica also show an increase in peaks at 1182, 1285, and 1423 cm⁻¹ with increasing power density. The band at 1182 cm⁻¹ has been previously reported as the C-H in plane bending; 41 however, 1285 cm⁻¹ is not commonly reported in the SERS spectrum of MBA. The peak at 1423 cm⁻¹ in the heatmaps suggest it arises from silica encapsulation as it is observed in the solution ensemble spectra in **Figure S1B.** The thiophenol associated peaks at 1000 and 1023 cm⁻¹ attributed to decarboxylation of MBA are observed to increase in intensity with increasing power density. These decarboxylation peaks are not observed at the lowest power density with the AuNP@silica particles, in contrast to the bare AuNPs (Figure 1A). Figure 4B-D show representative heat maps obtained at the lowest (5 kW/cm²), an intermediate (36 kW/cm²), and the highest power densities (195 kW/cm²). At the lowest power density (5 kW/cm²), it is difficult to identify any MBA peaks from AuNP@silica in individual acquisitions. The common MBA peaks at 1074 and 1590 cm⁻¹ are consistently present along with some frequency fluctuations in Figure 4C at 36 kW/cm². As the highest power density is reached at 195 kW/cm² the frequency fluctuations become more apparent and more intense as shown in Figure 4D.

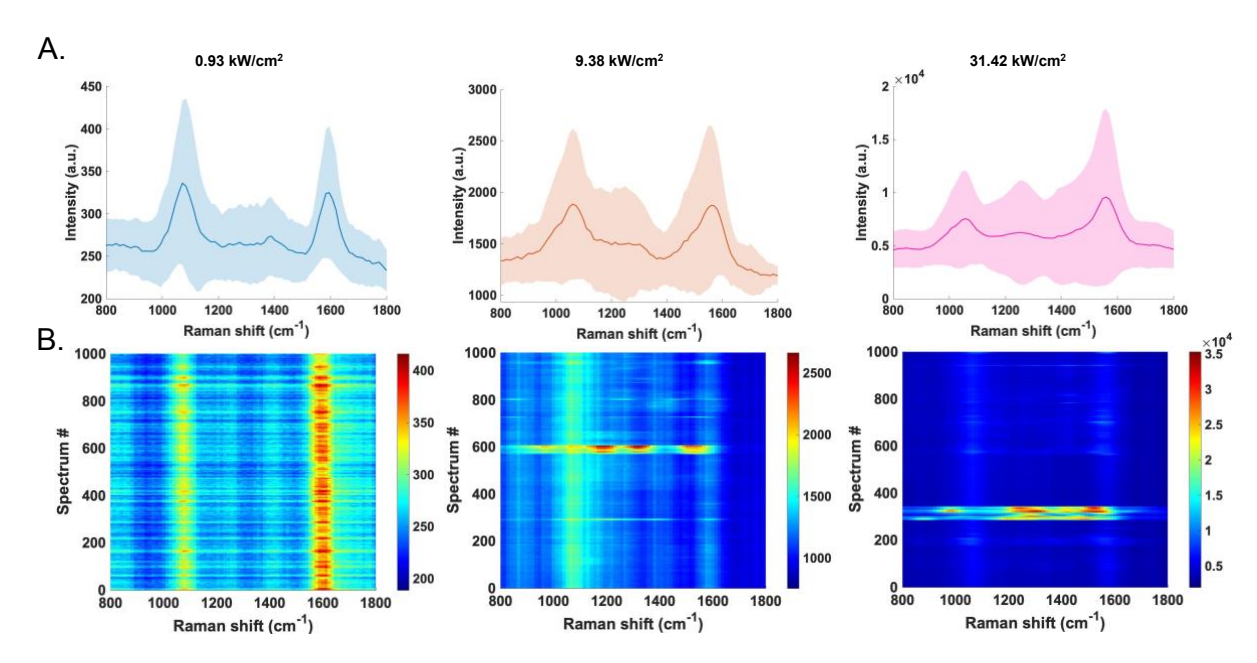


Figure 5: A) The mean spectrum obtained from MBA functionalized AuNP@silica particles at 0.93 (blue), 9.38 (orange), and 31.42 kW/cm² (pink) power densities are shown. The spectra shown are the average of 5 individual AuNP@silica particles, where 1000 acquisitions of 100 ms were acquired for each particle. B) A corresponding heat map showing frequency and intensity fluctuations from a representative particle (1000x, 100 ms acquisitions) at each power density is shown.

AuNP@silica particles were investigated using the wide field spectral imaging set-up to visualize individual particles and spectral fluctuations. At each power density, 1000 spectra were acquired for 100 ms each for each particle. **Figure 5A** shows the mean spectra derived from 5 particles (5000 spectra) at 3 different power densities, the lowest power density of 0.93 kW/cm² (blue), an intermediate power density of 9.38 kW/cm² (orange), and the highest power density of 31.42 kW/cm² (pink). At each power density, the average spectrum includes the prominent MBA peaks at 1074 and 1590 cm⁻¹. The standard deviation of the 5000 spectra is shown with each mean as a shaded region on the same plot. At the middle and highest power densities, the peaks in the average spectra begin to shift and broaden, indicating that spectra with intense fluctuations are present within the 5000 spectra comprising the average. With increasing power density, there is also an increase in the standard deviation of the spectra, which is common with SERS. In contrast to the AuNPs (**Figure 3A**), the AuNP@silica exhibit the expected MBA peaks at 1074 and 1590 cm⁻¹ in the mean spectra at all power densities.

Figure 5B shows a representative particle at each power density and shows an increase in the intensity of the spectral fluctuations with increasing power density. At a power density of 0.93 kW/cm², the only peaks are those associated with MBA at 1074 and 1590 cm⁻¹ with some intensity fluctuations of these peaks. As power density increases to 9.38 kW/cm², frequency fluctuations become more intense and are clear in the representative heat map in the middle of **Figure 5B**. After reaching the highest power density at 31.42 kW/cm², the intensity of the frequency fluctuations is approximately 10x more intense than at 9.38 kW/cm².

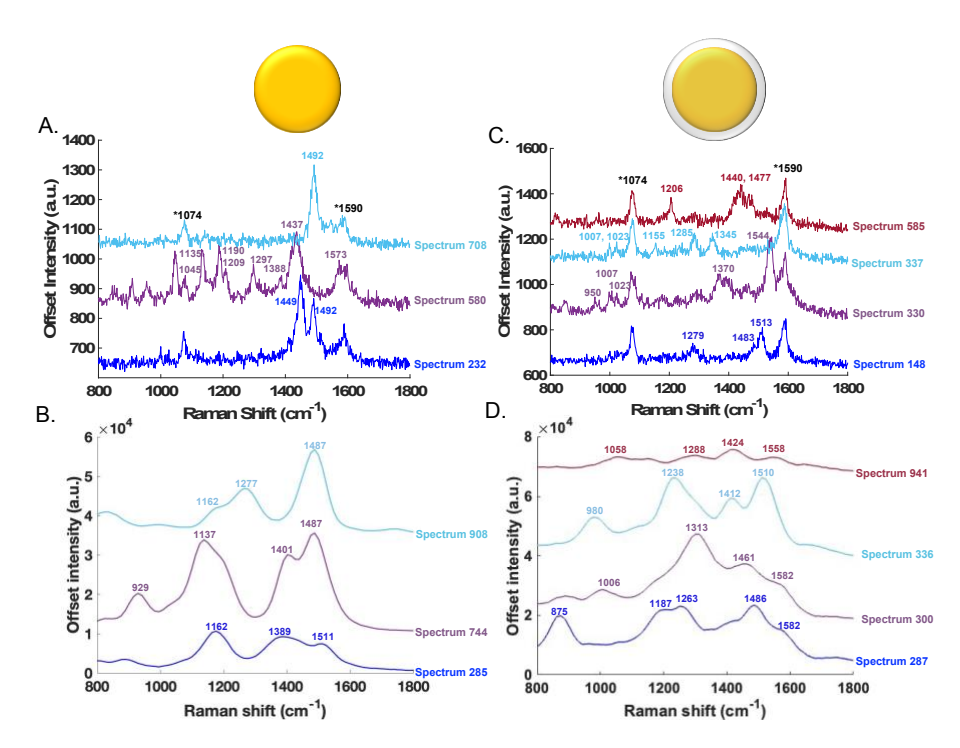


Figure 6: A comparison fluctuation spectra observed from: (A) point spectroscopy of AuNP (194 kW/cm²), (B) wide-field spectral imaging of AuNP (31 kW/cm²), (C) point spectroscopy of AuNP@silica particles (195 kW/cm²), and (D) wide-field spectral imaging of AuNP@silica particles (31 kW/cm²). The selected spectra highlight the fluctuations observed. Peak labels are included to facilitate comparison. Expected MBA peaks are labeled in black with a *. The spectrum number corresponds to the time point at which the spectrum was obtained. For example, spectrum 287 would be 2.87 s.

Analysis of the spectral fluctuations observed in both point spectroscopy data and widefield spectral imaging data suggest common patterns for MBA. Analysis was also completed with bare AuNP, presumably with the citrate capping agent present (Figure S8). The heat maps in Figure S8 show fluctuations can be observed from the citrate capping agent, however these frequency fluctuations are different from those observed with MBA functionalization at similar power densities for both point spectroscopy and wide-field spectral imaging. Figure 6 shows examples of individual spectra pulled from the highest power densities for each technique. Figure 6A shows spectra from 194 kW/cm² obtained using point spectroscopy. The peak energies are labeled and peaks corresponding with the expected MBA peaks are indicated with an asterisk in black. In the point spectra, the expected MBA peaks are observed at 1074 and 1590 cm⁻¹; however, these peaks are lower in intensity than the fluctuations. Figure 6B shows spectra obtained from 31.42 kW/cm² under wide field spectral imaging. The expected MBA peaks at 1074 and 1590 cm⁻ ¹ are not observed because of the strong intensity of the frequency fluctuations combined with the lower spectral resolution (Figure 3B). The frequency fluctuations shown in the spectra in Figure 6 can be associated with various transient species and photoproducts of MBA that have been previously reported. Our group has investigated MBA frequency fluctuations previously and have identified features that can be attributed to transient formation of the radical cation and radical anion based on density functional theory (DFT) calculations.²⁴ Our previous work suggests the MBA cation radical can be associated with peaks at 1189 and 1509 cm⁻¹. The same work shows the anion radical of MBA can be associated with peaks at 1283 and 1438 cm⁻¹. Peaks of similar frequency can be observed in point spectroscopy (Figure 6A) and in wide-field imaging (Figure

6B). Previously reported DFT simulations of the MBA anion and cation radicals Raman spectra²⁴ show agreement with these fluctuation spectra (**Figure S9**). Other fluctuation spectra in **Figure 6** contain peaks that are not associated with the radical cation or anion and suggest other intermediates.

The fluctuations in the spectra from the AuNP@silica particles show similar trends. In **Figure 6C** at 1.48 s, the intense shifted peak at 1513 cm⁻¹ is consistent with an previous reports of MBA frequency fluctuations.²⁴ This is within the spectral resolution of the peak at 1510 cm⁻¹ in **Figure 6D** from the wide field spectrum obtained at 33.6 s. Interestingly, fluctuations are also observed that could be correlated with the MBA anion radical. Radical anion peaks associated with MBA based on our previous work show up near 1283 and 1438 cm⁻¹. Peaks with consistent frequencies are observable in the point spectroscopy spectra shown in **Figure 6C**, as well as in the wide field spectrum in **Figure 6D**. The lower spectral resolution of the wide field spectral imaging broadens the spectral features, masking features with similar energy. We directly compare individual Raman spectra with the simulated radical anion and radical cation spectra in **Figure S9**, showing the overall spectral agreement. In the spectra obtained for the AuNP@silica, peaks associated with decarboxylation at 1007 and 1023 cm⁻¹ are evident at both 3.3 s and 3.37 s in **Figure 6A**. Fluctuating peaks that are not readily attributed to postulated intermediates are also observed, such as all the peaks in the spectrum at 28.7 and 94.1 s in **Figure 6D**.

Discussion.

The wide field spectral imaging experiment provides a high throughput method to assess frequency fluctuations associated with SIFs, but the decreased spectral resolution complicates assigning the observed fluctuations compared to point spectroscopy. For these reasons, combining the use of both point spectroscopy and wide-field spectral imaging can provide a better understanding of the fluctuations observed from the excitation of these gold nanoparticles.

Wide-field spectral imaging enables the determination of the fraction of particles experiencing frequency fluctuations at each power density and aids in identifying a threshold between sensing the expected MBA signals and the formation of photoproducts generated due to plasmon excitation. **Figure 7** plots the expected increase in fluctuating particles observed with increasing power density for both AuNP (red) and AuNP@silica (black). Over the range of power densities measured, the particles that were bright enough to be observed in the FOV were analyzed. The AuNP reached 100% of analyzed particles experiencing frequency fluctuations at a power density of 18.6 kW/cm² while the AuNP@silica reached 100% at 31.4 kW/cm². To determine a 50% and 10% threshold, a smooth spline fitting was applied to both data sets and is shown in **Figure 7** with the dotted lines. For the AuNP without silica, the 10% threshold is reached at 1.7 kW/cm² and the 50% threshold is reached at 5.7 kW/cm². The AuNP@silica reached the 10% threshold similarly at 1.9 kW/cm² however, the 50% threshold is not reached until 6.9 kW/cm². These differences are likely the result of the silica shell that encapsulated the MBA functionalized nanoparticle surfaces.

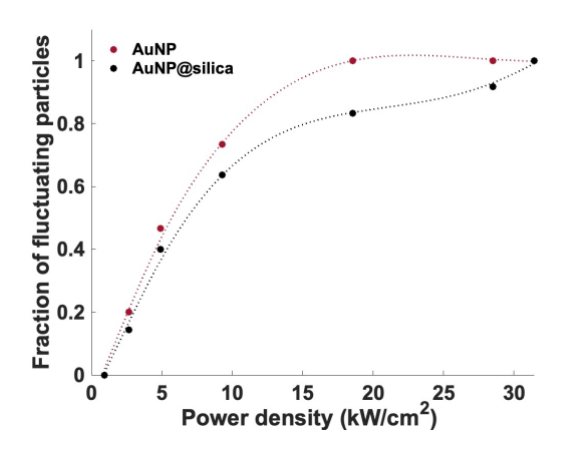


Figure 7: Plot of the fraction of particles, both AuNP (red) and AuNP@silica (black), exhibiting frequency fluctuations at each power density in the wide-field imaging experiments. A smooth spline fit was applied to both data sets to determine the 10% and 50% threshold of fluctuations. For the AuNP N=17, 15, 15, 15, 20, 24, 24 with increasing power density, and for AuNP@silica N=17, 14, 20, 22, 24, 24, 24 with increasing power density, respectively.

It is interesting to note the onset power of spectral fluctuations observed in the wide-field imaging experiments. In either case, greater than 50% of the particles show fluctuations at powers typical of SERS experiments, 100-150 μ W in the focused laser spot determined here. The change in the apparent onset of the frequency fluctuations in the AuNP@silica is consistent with added stability associated with a silica shell.⁴² This is consistent with the wide use of silica encapsulation for SERS-tags, where the stability of the chemical signal is key for sensing applications.⁴³⁻⁴⁴

Examining the fraction of particles expressing frequency fluctuations in the wide-field SERS imaging provides insight into the processes occurring. The lower power densities used in the wide-field imaging still evince frequency fluctuations. From the observed spatial image, we can infer the aggregation or isolation of particles which are providing spectral responses. For example, a single particle is expected to have a symmetric psf near the diffraction limit, while dimers and other aggregates will exhibit a larger and asymmetric psf (Figure S5). The psf information can be complemented by the polarization dependence (Figure S6) to differentiate symmetric isolated particles. Simultaneous information becomes extremely useful in the identification of the types of particles that are more likely to experience blinking and spectral fluctuations. Previous reports of nanoparticle aggregates, or decreased spacing between nanostructures, show hot carrier effects are more often exchanged between nanostructures rather than between the nanostructure to the molecule. 45-46 Interestingly, the psf of the fluctuating particles appear highly symmetric and are consistent with isolated particles, suggesting a higher incidence of hot carriers being captured by molecules on the surface rather than being transferred to adjacent particles. The wide-field imaging allows us to detect more isolated particles to track hot carrier transfer to MBA specifically. The intensity of the frequency fluctuations is typically more intense than the normal MBA spectra, which may help identify single particles.

There have been reports that suggest individual nanoparticles are not detectable in SERS.⁴⁷ In fact, in our point spectroscopy experiments, the observed frequency fluctuations are most evident at much higher laser powers. One explanation for this is our point spectroscopy data originates from aggregated particles. While fluctuations are observed, they are less intense than

observed in the wide-field experiments. This is consistent with the hypothesis that energetic carriers prefer to transfer between particles rather than to molecules. The more consistent spectral response arises from the increased field, while the capture of energetic charge carriers is less influential. Reporting the mean spectral response can overwhelm the signals from transient species that are the result of hot-carrier transfer. This agrees with prior reports showing how transient SERS signals are lost when long signal acquisitions are used.⁴⁸⁻⁴⁹ In our data, features in the mean ensemble spectra indicative of transient hot-carrier species, as well as photodamage and photoconversion with increasing power, can often be overlooked when they are low intensity compared to the expected Raman signal for detection.

Assigning the spectral fluctuations becomes incredibly important for chemical identification of transient species, which could provide insight into reaction pathways. In **Figure S9**, we have identified spectral examples of fluctuation data that correlate to previously simulated Raman spectra of radical cation and radical anion formation of MBA.²⁴ Other reports of radical formation through plasmonic hot-carrier formation support the possibility of this type of hot-carrier species.²⁷⁻²⁹ In addition to radical formation, other transient species can be identified as products of photodamage from hot carriers. The formation of thiophenol from plasmonically induced conversion of MBA has been reported to result in the formation of peaks at 998, 1022, and 1572 cm⁻¹ which are features we also observe with increasing laser power.⁵⁰ Formation of radical species are examples of transient species, while the conversion of MBA to thiophenol represents a reaction product. We are unable to account for all the transient peaks observed, but further analysis may reveal the nature of the photochemical reactions occurring.

Conclusion

The combination of wide-field imaging and point spectroscopy allows for monitoring of hot-carriers interacting with molecules on the surface of plasmonic particles. Transient species are observed at low power densities from nanostructures that are consistent with isolated nanoparticles. These low power density events are difficult to capture in point spectroscopy measurements, where the observed signals appear to arise from aggregates. Comparing the spectral information from point spectroscopy with the spectral features observed in wide-field imaging suggests molecular origins for the fluctuating frequencies that can then be readily compared to simulated spectra from DFT calculations to identify transient species, such as radicals. Our results suggest that isolated particles may be more active for chemical conversion while these carriers are quenched in aggregates. While here we have identified a few intermediate species that appear transiently for MBA under plasmonic excitation of hot carriers, there remains a need to understand all transient spectral fluctuations. Additional analysis and correlation to electron microscopy may provide new insight into chemical processes relevant to catalysts as well as optimizing sensors.

Acknowledgment.

This work was supported by the National Science Foundation Award CHE- 2107791 and the National Institutes of Health Award R01-GM109988 to ZDS. CMZ and DNS were supported by NSF Award CHE-2107791. The authors thank Brian Scarpitti for synthesis of the silica encapsulated nanoparticles, which were produced as part of R01-GM109988. The Authors

acknowledge Zac O'Dell for insightful discussion about the polarization dependence in SERS imaging.

Supporting Information Available: Supporting Figures S1 - S9 are available showing further characterization of the samples and additional results imaging and spectroscopy experiments. Supporting videos are available showing the signal fluctuations at power densities of 0.9 kW/cm^2 and 31 kW/cm^2 .

References:

- 1. Langer, J.; Jimenez de Aberasturi, D.; Aizpurua, J.; Alvarez-Puebla, R. A.; Auguié, B.; Baumberg, J. J.; Bazan, G. C.; Bell, S. E. J.; Boisen, A.; Brolo, A. G., et al., Present and Future of Surface-Enhanced Raman Scattering. *ACS Nano* **2019**, *14*, 28-117.
- 2. Zhang, Z.; Zhang, C.; Zheng, H.; Xu, H., Plasmon-Driven Catalysis on Molecules and Nanomaterials. *Accounts of Chemical Research* **2019**, *52*, 2506-2515.
- 3. Zhou, X. L.; Yang, Y.; Wang, S.; Liu, X. W., Surface Plasmon Resonance Microscopy: From Single-Molecule Sensing to Single-Cell Imaging. *Angewandte Chemie International Edition* **2020**, *59*, 1776-1785.
- 4. Tabasi, O.; Falamaki, C., Recent Advancements in the Methodologies Applied for the Sensitivity Enhancement of Surface Plasmon Resonance Sensors. *Analytical Methods* **2018**, *10*, 3906-3925.
- 5. Jeanmaire, D. L.; Van Duyne, R. P., Surface Raman Spectroelectrochemistry. *Journal of Electroanalytical Chemistry and Interfacial Electrochemistry* **1977**, *84*, 1-20.
- 6. Fleischmann, M.; Hendra, P. J.; McQuillan, A. J., Raman Spectra of Pyridine Adsorbed at a Silver Electrode. *Chemical Physics Letters* **1974**, *26*, 163-166.
- 7. Moskovits, M., Surface Roughness and the Enhanced Intensity of Raman Scattering by Molecules Adsorbed on Metals. *The Journal of Chemical Physics* **1978**, *69*, 4159-4161.
- 8. Mukherjee, S.; Libisch, F.; Large, N.; Neumann, O.; Brown, L. V.; Cheng, J.; Lassiter, J. B.; Carter, E. A.; Nordlander, P.; Halas, N. J., Hot Electrons Do the Impossible: Plasmon-Induced Dissociation of H2 on Au. *Nano Letters* **2012**, *13*, 240-247.
- 9. Zhou, L.; Swearer, D. F.; Zhang, C.; Robatjazi, H.; Zhao, H.; Henderson, L.; Dong, L.; Christopher, P.; Carter, E. A.; Nordlander, P., et al., Quantifying Hot Carrier and Thermal Contributions in Plasmonic Photocatalysis. *Science* **2018**, *362*, 69-72.
- 10. Yu, S.; Jain, P. K., The Chemical Potential of Plasmonic Excitations. *Angewandte Chemie International Edition* **2020**, *59*, 2085-2088.
- 11. Linic, S.; Chavez, S.; Elias, R., Flow and Extraction of Energy and Charge Carriers in Hybrid Plasmonic Nanostructures. *Nature Materials* **2021**, *20*, 916-924.
- Wang, X.; Huang, S.-C.; Hu, S.; Yan, S.; Ren, B., Fundamental Understanding and Applications of Plasmon-Enhanced Raman Spectroscopy. *Nature Reviews Physics* **2020**, *2*, 253-271.
- 13. Zhang, Y.; He, S.; Guo, W.; Hu, Y.; Huang, J.; Mulcahy, J. R.; Wei, W. D., Surface-Plasmon-Driven Hot Electron Photochemistry. *Chem. Rev.* **2018**, *118*, 2927-2954.
- 14. Linic, S.; Aslam, U.; Boerigter, C.; Morabito, M., Photochemical Transformations on Plasmonic Metal Nanoparticles. *Nature Materials* **2015**, *14*, 567-576.
- 15. Kneipp, K., Chemical Contribution to Sers Enhancement: An Experimental Study on a Series of Polymethine Dyes on Silver Nanoaggregates. *The Journal of Physical Chemistry C* **2016**, *120*, 21076-21081.
- 16. Mittal, D.; Ahlawat, M.; Govind Rao, V., Recent Progress and Challenges in Plasmon-Mediated Reduction of CO₂ to Chemicals and Fuels. *Advanced Materials Interfaces* **2022**, *9*, 2102383.
- 17. Landaeta, E.; Masitas, R. A.; Clarke, T. B.; Rafacz, S.; Nelson, D. A.; Isaacs, M.; Schultz, Z. D., Copper-Oxide-Coated Silver Nanodendrites for Photoelectrocatalytic CO₂ Reduction to Acetate at Low Overpotential. *ACS Applied Nano Materials* **2020**, *3*, 3478-3486.

- 18. Huang, Y.-F.; Zhu, H.-P.; Liu, G.-K.; Wu, D.-Y.; Ren, B.; Tian, Z.-Q., When the Signal Is Not from the Original Molecule to Be Detected: Chemical Transformation of Para-Aminothiophenol on Ag During the Sers Measurement. *Journal of the American Chemical Society* **2010**, *132*, 9244-9246.
- 19. Fang, Y.; Li, Y.; Xu, H.; Sun, M., Ascertaining P,P'-Dimercaptoazobenzene Produced from P-Aminothiophenol by Selective Catalytic Coupling Reaction on Silver Nanoparticles. *Langmuir* **2010**, *26*, 7737-7746.
- 20. Burtsev, V.; Miliutina, E.; Ulbrich, P.; Elashnikov, R.; Svorcik, V.; Orendac, M.; Lyutakov, O., Immobilization of Gold Nanoparticles in Localized Surface Plasmon Polariton-Coupled Hot Spots Via Photolytic Dimerization of Aromatic Amine Groups for Detection in a Microfluidic Regime. *ACS Applied Nano Materials* **2022**, *5*, 1836-1844.
- 21. Wang, R.; Li, J.; Rigor, J.; Large, N.; El-Khoury, P. Z.; Rogachev, A. Y.; Kurouski, D., Direct Experimental Evidence of Hot Carrier-Driven Chemical Processes in Tip-Enhanced Raman Spectroscopy (Ters). *The Journal of Physical Chemistry C* **2020**, *124*, 2238-2244.
- 22. Yamamoto, Y. S.; Ishikawa, M.; Ozaki, Y.; Itoh, T., Fundamental Studies on Enhancement and Blinking Mechanism of Surface-Enhanced Raman Scattering (Sers) and Basic Applications of Biological Sensing. *Frontiers of Physics* **2013**, *9*, 31-46.
- dos Santos, D. P.; Temperini, M. L. A.; Brolo, A. G., Intensity Fluctuations in Single-Molecule Surface-Enhanced Raman Scattering. *Accounts of Chemical Research* **2019**, *52*, 456-464.
- 24. de Albuquerque, C. D. L.; Zoltowski, C. M.; Scarpitti, B. T.; Shoup, D. N.; Schultz, Z. D., Spectrally Resolved Surface-Enhanced Raman Scattering Imaging Reveals Plasmon-Mediated Chemical Transformations. *ACS Nanoscience Au* **2021**, *1*, 38-46.
- 25. Zhang, W.; Caldarola, M.; Pradhan, B.; Orrit, M., Gold Nanorod Enhanced Fluorescence Enables Single-Molecule Electrochemistry of Methylene Blue. *Angewandte Chemie International Edition* **2017**, *56*, 3566-3569.
- 26. Clément, J.-E.; Leray, A.; Bouhelier, A.; Finot, E., Spectral Pointillism of Enhanced Raman Scattering for Accessing Structural and Conformational Information on Single Protein. *Physical Chemistry Chemical Physics* **2017**, *19*, 458-466.
- 27. Zoltowski, C. M.; Lalisse, R. F.; Hadad, C. M.; Schultz, Z. D., Plasmonically Generated Tryptophan Radical Anion on Gold Nanoparticles Investigated by Combined Surface-Enhanced Raman Scattering and Density Functional Theory Calculations. *The Journal of Physical Chemistry C* **2021**, *125*, 27596-27606.
- 28. Sprague-Klein, E. A.; Negru, B.; Madison, L. R.; Coste, S. C.; Rugg, B. K.; Felts, A. M.; McAnally, M. O.; Banik, M.; Apkarian, V. A.; Wasielewski, M. R., et al., Photoinduced Plasmon-Driven Chemistry in Trans-1,2-Bis(4-Pyridyl)Ethylene Gold Nanosphere Oligomers. *J. Am. Chem. Soc.* **2018**, *140*, 10583-10592.
- 29. Sprague-Klein, E. A.; McAnally, M. O.; Zhdanov, D. V.; Zrimsek, A. B.; Apkarian, V. A.; Seideman, T.; Schatz, G. C.; Van Duyne, R. P., Observation of Single Molecule Plasmon-Driven Electron Transfer in Isotopically Edited 4,4'-Bipyridine Gold Nanosphere Oligomers. *Journal of the American Chemical Society* **2017**, *139*, 15212-15221.
- 30. Sprague-Klein, E. A.; Ho-Wu, R.; Nguyen, D.; Coste, S. C.; Wu, Y.; McMahon, J. J.; Seideman, T.; Schatz, G. C.; Van Duyne, R. P., Modulating the Electron Affinity of Small Bipyridyl Molecules on Single Gold Nanoparticles for Plasmon-Driven Electron Transfer. *The Journal of Physical Chemistry C* **2021**, *125*, 22142-22153.
- 31. Wang, H.; Yao, K.; Parkhill, J. A.; Schultz, Z. D., Detection of Electron Tunneling across Plasmonic Nanoparticle–Film Junctions Using Nitrile Vibrations. *Physical Chemistry Chemical Physics* **2017**, *19*, 5786-5796.
- 32. Payton, J. L.; Morton, S. M.; Moore, J. E.; Jensen, L., A Hybrid Atomistic Electrodynamics—Quantum Mechanical Approach for Simulating Surface-Enhanced Raman Scattering. *Accounts of Chemical Research* **2013**, *47*, 88-99.

- 33. Zeng, Z.-C.; Wang, H.; Johns, P.; Hartland, G. V.; Schultz, Z. D., Photothermal Microscopy of Coupled Nanostructures and the Impact of Nanoscale Heating in Surface-Enhanced Raman Spectroscopy. *The Journal of Physical Chemistry C* **2017**, *121*, 11623-11631.
- 34. Wustholz, K. L.; Henry, A.-I.; McMahon, J. M.; Freeman, R. G.; Valley, N.; Piotti, M. E.; Natan, M. J.; Schatz, G. C.; Van Duyne, R. P., Structure–Activity Relationships in Gold Nanoparticle Dimers and Trimers for Surface-Enhanced Raman Spectroscopy. *Journal of the American Chemical Society* **2010**, *132*, 10903-10910.
- 35. Kimling, J.; Maier, M.; Okenve, B.; Kotaidis, V.; Ballot, H.; Plech, A., Turkevich Method for Gold Nanoparticle Synthesis Revisited. *The Journal of Physical Chemistry B* **2006**, *110*, 15700-15707.
- 36. Shoup, D. N.; Scarpitti, B. T.; Schultz, Z. D., A Wide-Field Imaging Approach for Simultaneous Super-Resolution Surface-Enhanced Raman Scattering Bioimaging and Spectroscopy. *ACS Measurement Science Au* **2022**, 10.1021/acsmeasuresciau.2c00013.
- 37. Szczerbiński, J.; Gyr, L.; Kaeslin, J.; Zenobi, R., Plasmon-Driven Photocatalysis Leads to Products Known from E-Beam and X-Ray-Induced Surface Chemistry. *Nano Lett* **2018**, *18*, 6740-6749.
- 38. Scarpitti, B. T.; Morrison, A. M.; Buyanova, M.; Schultz, Z. D., Comparison of 4-Mercaptobenzoic Acid Surface-Enhanced Raman Spectroscopy-Based Methods for Ph Determination in Cells. *Appl. Spectrosc.* **2020**, *74*, 1423-1432.
- 39. Puppulin, L.; Hosogi, S.; Sun, H.; Matsuo, K.; Inui, T.; Kumamoto, Y.; Suzaki, T.; Tanaka, H.; Marunaka, Y., Bioconjugation Strategy for Cell Surface Labelling with Gold Nanostructures Designed for Highly Localized Ph Measurement. *Nature Communications* **2018**, *9*, 5278.
- 40. Capocefalo, A.; Mammucari, D.; Brasili, F.; Fasolato, C.; Bordi, F.; Postorino, P.; Domenici, F., Exploring the Potentiality of a SERS-Active Ph Nano-Biosensor. *Front Chem* **2019**, *7*, 413.
- 41. Liu, Y.; Yuan, H.; Fales, A. M.; Vo-Dinh, T., Ph-Sensing Nanostar Probe Using Surface-Enhanced Raman Scattering (SERS): Theoretical and Experimental Studies. *Journal of Raman Spectroscopy* **2013**, *44*, 980-986.
- 42. Cui, Y.; Zheng, X.-S.; Ren, B.; Wang, R.; Zhang, J.; Xia, N.-S.; Tian, Z.-Q., Au@Organosilica Multifunctional Nanoparticles for the Multimodal Imaging. *Chemical Science* **2011**, *2*, 1463.
- 43. Li, C.-Y.; Meng, M.; Huang, S.-C.; Li, L.; Huang, S.-R.; Chen, S.; Meng, L.-Y.; Panneerselvam, R.; Zhang, S.-J.; Ren, B., et al., "Smart" Ag Nanostructures for Plasmon-Enhanced Spectroscopies. *Journal of the American Chemical Society* **2015**, *137*, 13784-13787.
- 44. Goodacre, R.; Graham, D.; Faulds, K., Recent Developments in Quantitative SERS: Moving Towards Absolute Quantification. *TrAC Trends in Analytical Chemistry* **2018**, *102*, 359-368.
- 45. Zhang, Y.; Nelson, T.; Tretiak, S.; Guo, H.; Schatz, G. C., Plasmonic Hot-Carrier-Mediated Tunable Photochemical Reactions. *ACS Nano* **2018**, *12*, 8415-8422.
- 46. Cortes, E.; Xie, W.; Cambiasso, J.; Jermyn, A. S.; Sundararaman, R.; Narang, P.; Schlucker, S.; Maier, S. A., Plasmonic Hot Electron Transport Drives Nano-Localized Chemistry. *Nat Commun* **2017**, *8*, 14880.
- 47. Zhang, Z.; Bando, K.; Mochizuki, K.; Taguchi, A.; Fujita, K.; Kawata, S., Quantitative Evaluation of Surface-Enhanced Raman Scattering Nanoparticles for Intracellular Ph Sensing at a Single Particle Level. *Anal. Chem.* **2019**, *91*, 3254-3262.
- 48. Scott, B. L.; Carron, K. T., Dynamic Surface Enhanced Raman Spectroscopy (SERS): Extracting SERS from Normal Raman Scattering. *Anal. Chem.* **2012**, *84*, 8448-8451.
- 49. Asiala, S. M.; Schultz, Z. D., Label-Free in Situ Detection of Individual Macromolecular Assemblies by Surface Enhanced Raman Scattering. *Chem. Commun.* **2013**, *49*, 4340-4342.
- 50. Zong, Y.; Guo, Q.; Xu, M.; Yuan, Y.; Gu, R.; Yao, J., Plasmon-Induced Decarboxylation of Mercaptobenzoic Acid on Nanoparticle Film Monitored by Surface-Enhanced Raman Spectroscopy. *RSC Adv.* **2014**, *4*, 31810-31816.

TOC Figure:

